

A novel method for component separation of extended sources in X-ray astronomy

A. Picquenot¹, F. Acero¹, J. Bobin¹, P. Maggi², J. Ballet¹, and G.W. Pratt¹

¹ AIM, CEA, CNRS, Université Paris-Saclay, Université Paris Diderot, Sorbonne Paris Cité, F-91191 Gif-sur-Yvette, France e-mail: adrien.picquenot@cea.fr, fabio.acero@cea.fr

² Observatoire Astronomique de Strasbourg, Université de Strasbourg, CNRS, 11 rue de l'Université, F-67000 Strasbourg, France

Thursday 14th March, 2019

ABSTRACT

In high-energy astronomy, spectro-imaging instruments such as X-ray detectors allow investigation of the spatial and spectral properties of extended sources including galaxy clusters, galaxies, diffuse interstellar medium, supernova remnants and pulsar wind nebulae. In these sources, each physical component possesses a different spatial and spectral signature, but the components are entangled. Extracting the intrinsic spatial and spectral information of the individual components from this data is a challenging task. Current analysis methods do not fully exploit the 2D-1D (x, y, E) nature of the data, as the spatial and spectral information are considered separately. Here we investigate the application of a Blind Source Separation (BSS) algorithm that jointly exploits the spectral and spatial signatures of each component in order to disentangle them. We explore the capabilities of a new BSS method (the General Morphological Component Analysis; GMCA), initially developed to extract an image of the Cosmic Microwave Background from *Planck* data, in an X-ray context. The performance of the GMCA on X-ray data is tested using Monte-Carlo simulations of supernova remnant toy models, designed to represent typical science cases. We find that the GMCA is able to separate highly entangled components in X-ray data even in high contrast scenarios, and can extract with high accuracy the spectrum and map of each physical component. A modification of the algorithm is proposed in order to improve the spectral fidelity in the case of strongly overlapping spatial components, and we investigate a resampling method to derive realistic uncertainties associated to the results of the algorithm. Applying the modified algorithm to the deep *Chandra* observations of Cassiopeia A, we are able to produce detailed maps of the synchrotron emission at low energies (0.6–2.2 keV), and of the red/blue shifted distributions of a number of elements including Si and Fe K.

Key words.

1. Introduction

Beginning in the 1970s, it was realised that the X-ray sky is full of extended sources, among which we find emission from the Milky Way itself, other Galactic sources such as pulsar wind nebulae or supernova remnants (SNRs), and extragalactic sources such as galaxies and clusters of galaxies. The typical emission components one can see in X-rays from these types of objects are thermal emission, or accelerated particles radiating through the synchrotron process. In each case, their spectral signature is distinctive and recognizable. For example, in SNRs the shock wave propagating rapidly through the interstellar medium heats it up to approximately 10^7 K, resulting in thermal emission peaking in the X-ray domain.

Spectro-imaging instruments such as those aboard the current generation of X-ray satellites *XMM-Newton* and *Chandra* provide data comprising spatial and spectral information: the detectors record the position (x, y) and energy E event by event, thereby providing a data cube with two spatial dimensions and one spectral dimension.

An ability to disentangle in this 2D-1D data cube the different physical components would allow us to learn more about their respective spatial and spectral distributions. However, the different components are frequently superimposed along the line of sight, or are even physically nested, making such separation difficult.

In this paper we introduce a new method to disentangle spectral components from X-ray data of extended sources. Separating a set of components mixed in a set of observations is known in signal processing as a blind source separation (BSS) problem. Our method is based on an algorithm that uses the ability of wavelets to provide a sparse representation for astrophysical images to find a solution to BSS problems. In this context, we consider our 2D-1D data cube as the product between an image and a spectrum. This algorithm, the Generalized Morphological Components Analysis (GMCA), was first developed by Bobin et al. (2015), and has recently been applied to *Planck* survey data to separate the image of the Cosmic Microwave Background (CMB) from the foregrounds (Bobin et al. 2016). The application of the GMCA method to X-ray data is non-trivial. While in *Planck* the data are obtained in nine fixed frequencies, the X-ray photons can be binned into an arbitrarily large number of energy bins; the X-ray photon count is drastically lower at high energies, and has higher dynamic range. In addition, the X-ray data have Poisson noise whereas the GMCA method assumes an additive Gaussian noise.

Here we adapt the GMCA algorithm to the study of extended sources in X-rays, and test its implementation by applying the method to SNR data. We first test the method on toy models reproducing X-ray data of SNRs containing up to three components (see Sections 4 and 7). Although the noise is Poissonian in our simulated data set, we have obtained accurate spectral shapes

26
27
28
29
30
31
32
33
34
35
36
37
38
39
40
41
42
43
44
45
46
47
48
49
50
51

52 and cleaner images than with any of the typical X-ray analysis
 53 techniques. However, we find that a strong spatial correlation
 54 between the components leads to a leakage from the main com-
 55 ponents to the weaker ones, which may be partially linked to the
 56 nature of the noise, and we implement a refinement step in the
 57 algorithm to minimize this effect (see Section 5). Although a ver-
 58 sion of the GMCA handling Poisson statistics is currently being
 59 developed, our results show that the existing version can be used
 60 to disentangle extended sources in X-rays. Applying our method
 61 to real data from the Cassiopeia A SNR yields sharp images of
 62 the synchrotron at low and high energy, and images of the dis-
 63 tributions of a number of elements including Si and Fe K (see
 64 Section 8). In both cases, one of the images presents the blue-
 65 shifted part of the structure, and the other one the red-shifted
 66 part.

67 2. Motivations and current methods

68 The telescopes *XMM-Newton* and *Chandra* have provided a ma-
 69 jor step forward in effective area and angular resolution, and
 70 led to nearly 20 years of observations resulting in deep (Mega-
 71 seconds) archival public datasets. As an example, the deep *Chan-
 72 dra* ~ 2 Ms observation of SNR Cassiopeia A resulted in about
 73 a billion X-ray photons. Despite this breakthrough improvement
 74 in data quality, the analysis techniques used to extract the wealth
 75 of information contained in such datasets have stalled.

76 The main analysis challenge lies in the fact that at each po-
 77 sition, the different spectral components (e.g. synchrotron and
 78 thermal emission from the shocked medium and ejecta) are pro-
 79 jected along the line of sight, and that the observed signal is a
 80 combination of these components.

81 In the study of SNRs, a typical scientific case is to study
 82 the spatial distribution of a spectral feature (e.g. heavy elements
 83 maps to probe the morphology and asymmetries of the ejecta).
 84 The common methods are to generate maps integrated around
 85 the centroid energy of a line and to subtract the underlying con-
 86 tinuum estimated from adjacent energy bands (the continuum
 87 interpolation method). However, if the faint emission lines are
 88 dominated by the continuum or if the adjacent energies also have
 89 emission lines, those methods perform poorly. An alternative
 90 method to study the spatial variations of the spectral properties is
 91 to divide the image into subregions and carry out a spectral anal-
 92 ysis in each subregion. One frequently-used method is to define
 93 regions of equal photon statistics with for example the Voronoï
 94 tiling method (see Diehl & Statler 2006, for an adaptation to
 95 X-rays). Each cell is then fitted with a physical model indepen-
 96 dently from its neighbors and maps representing the best-fit pa-
 97 rameters are produced. This method is time consuming and does
 98 not take into account the underlying relationship between the
 99 spatial and spectral components. In addition, the best-fit pa-
 100 rameter map may suffer from statistical fluctuations from cell to cell
 101 as for practical reasons only one grid is defined using a reference
 102 image in a large energy range that might not represent the flux
 103 of individual spectral components.

104 To summarize, one of the root issues of the methods de-
 105 scribed above is that each region (pixels or cell) is treated inde-
 106 pendently. The disentangling process only relies on the spectral
 107 signature of the components in each region considered, whereas
 108 in reality the physical components also have different spatial sig-
 109 natures. Exploiting both the spectral and spatial signatures of the
 110 components and treating pixels not individually but as a whole
 111 yields more discriminative power to disentangle the different
 112 physical components. We note that other methods such as the
 113 Principal Component Analysis (PCA) have already been applied

to SNRs in the past to retrieve entangled components (see Warren et al. 2005). However, the PCA works in such a way that it
 114 has to retrieve decorrelated components, which usually makes
 115 them not physically significant. We can also cite Jones et al.
 116 (2015), that used Bayesian statistical methods to infer the num-
 117 ber of sources and probabilistically separate photons among the
 118 sources. Yet, these methods work with event lists (x, y, E) , and
 119 do not retrieve images or spectra associated with the sources, as
 120 our method does.
 121

122 3. A Blind Source Separation method: the GMCA

123 3.1. Description of the method

Blind source separation methods aim to disentangle mixed
 124 sources in a data set without prior information. A classic way
 125 to do so, is to look at the original data in a mathematical space
 126 where the sources will be sufficiently different from one another.
 127 The concept of sparsity helps to determine what kind of space
 128 could be suitable: a sparse signal is a signal in which most of the
 129 coefficients are zero. Thus, two sparse signals will be easier to
 130 disentangle as their signatures will not be correlated. For exam-
 131 ple, to separate periodic signals in a unidimensional data set, it
 132 is much easier to work in Fourier space, where such sources will
 133 be entirely determined by a few coefficients.
 134

In this paper, we introduce a new method to disentangle
 135 physical components based on their spatial and spectral signa-
 136 ture. This method is based on the Generalized Morphological
 137 Components Analysis (GMCA) algorithm, a blind source sep-
 138 aration algorithm developed to disentangle the CMB from the
 139 galactic foregrounds in the data of the *Planck* satellite (Bobin
 140 et al. 2015). The input is a data cube (E, x, y) , where E is the
 141 spectral dimension and x and y are spatial dimensions.
 142

The main concept of GMCA is to take into account the
 143 morphological particularities of each component to disentangle
 144 them. Apart from the (E, x, y) data cube, the only input needed is
 145 the number n of components to retrieve, which is user-defined.
 146 To optimize the disentangling process, the signal is projected in
 147 a space where it will have a sparse representation. Thus, two
 148 components that are sufficiently different spatially will have few
 149 coefficients in common, allowing us to separate them more eas-
 150 iily. In the case of images, the equivalent of the Fourier space
 151 would be a correctly chosen wavelet transform, that would con-
 152 centrate most of the image information into a few coefficients
 153 (for more about wavelets, and for an illustration of the interest
 154 of the wavelet space to disentangle components in a data cube
 155 (E, x, y) , see Appendix A).
 156

157 3.2. Mathematical formalism

Here we will use the undecimated¹ Starlet transform (see Starck
 159 et al. 2007, and Appendix A) which is well suited for astronom-
 160 ical purposes. Each wavelet scale contains information about
 161 structures of a specific size, which allows us to isolate more
 162 easily the morphological features of each component. In order
 163 to minimize cross-correlations between components, the two
 164 largest wavelet scales are not used, because in these scales mor-
 165 phological features are harder to differentiate.
 166

For a data cube of dimension (E, x, y) , we apply a wavelet
 167 transform with J scales on the images of each energy slice of
 168 the cube resulting in an array X of dimension $(E, x, y, J - 2)$,

¹ An undecimated transform produces images of the same size for each scale.

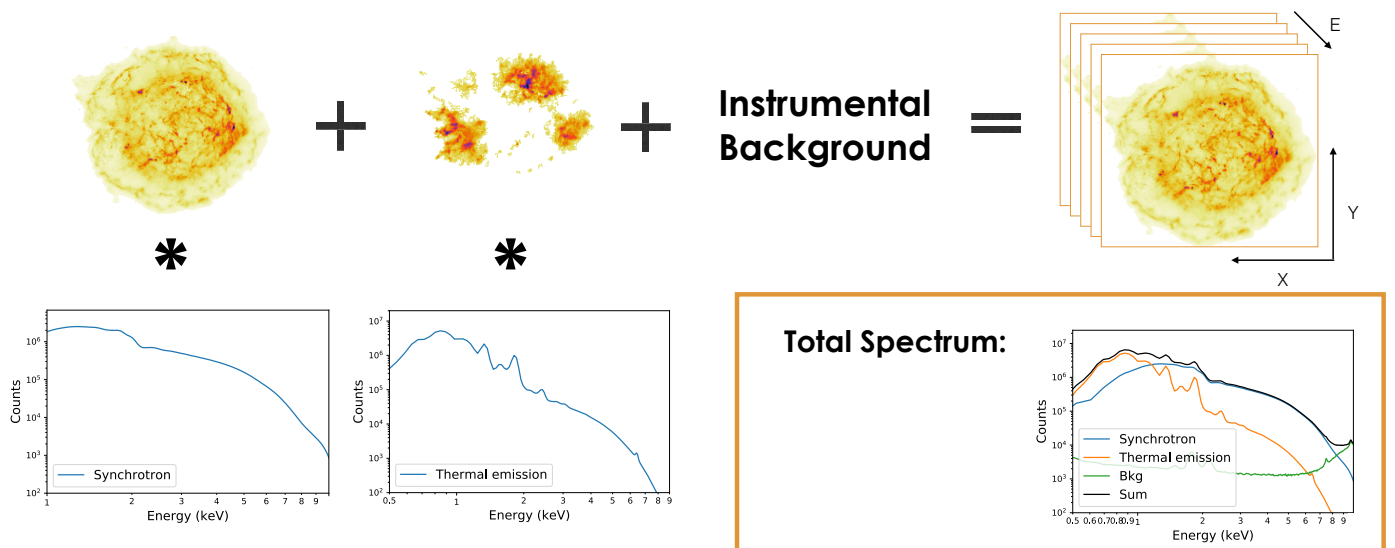


Fig. 1: A presentation of our toy model, consisting in the sum of images multiplied by theoretical spectra. The spatial distribution of the instrumental background is uniform.

the two largest wavelets scales being rejected. We note that the wavelet transform is applied only on images, and that there is no constraint on the sparsity of the spectra. The aim of the GMCA is to solve the following problem:

$$X = AS + N = \sum_{i=1}^n A_i S_i + N \quad (1)$$

where n is the predefined number of components, the A_i are vectors of size E , in our case related to the spectral information (the spectra of our mixed components), the S_i are the sources represented in wavelets, of dimension (x, y, J) and related to the spatial information (the images in wavelets of our mixed components), and N is a Gaussian noise. The product here for a given i is the multiplication of every coefficient of A_i by every coefficient of S_i . The components to retrieve are assumed to be modeled as the product of an image (S_i in the wavelet space) and a spectrum (A_i). Thus, the retrieved components are approximations of the actual components with the same spectrum on each point of the image. This problem being an ill-posed inverse problem, as both A and S are unknown, one needs a constraint to solve it. The GMCA relies on the assumption that, once the image has been translated into wavelet space, each constituent can be sparsely represented, thus making the component separation easier.

The GMCA solves the inverse problem by imposing a sparsity constraint: it maximizes the sparsity of the images of each source in the wavelet domain. The problem being actually solved by the GMCA is thus the following optimization problem:

$$\min_{A, S} \sum_{i=1}^n \lambda_i \|S_i\|_p + \|X - AS\|_F^2 \quad (2)$$

where λ_i are regularization coefficients equivalent to thresholds that aim at rejecting noise samples, and prove essential to provide robustness with respect to noise. They are chosen thanks

to an estimation of the noise level in the sources based on the Median Absolute Deviation (MAD) method, and progressively decrease towards the final noise-related level. $\|\cdot\|_F$ is the Frobenius norm defined by $\|Y\|_F^2 = \text{Trace}(YY^T)$ and $\|\cdot\|_p$ is a l_p norm, with $p = 0$ or $p = 1$. The l_1 norm is defined by $\|Y\|_1 = \sum_{i,j} |Y_{i,j}|$ and $\|Y\|_0$ counts the number of non-zero entries in Y . The l_0 and l_1 norms are customarily used to measure the sparsity of signals. The first term of this equation is a sparsity constraint term and the second is a data-fidelity term.

More precisely, the GMCA is an iterative algorithm repeating the following two steps :

- Step 1: Estimation of S for fixed A , by simultaneously minimizing $\|X - AS\|_F$ and the term enforcing sparsity in the Wavelet domain;
- Step 2: Estimation of A for fixed S by minimizing $\|X - AS\|_F$.

3.3. Application of the method

When the GMCA was applied to *Planck* data, its original purpose, the CMB spectrum was fixed to its theoretical shape. Giving a known spectrum as additional information fixes a column in A , making the algorithm work in what is termed a *semi-blind* mode. However, if the theoretical spectrum is not previously known, the algorithm can also work in a completely *blind* mode. With our toy model example (described in the next Section), we test both of these modes.

The only input needed is the number n of components to retrieve. Any prior knowledge of the data can help to choose n wisely, as the expected number of components visible in the energy band on which the GMCA is applied. In addition, this algorithm is running fast (a few minutes to extract sources from a 200*200*300 single core personal computer), so we highly recommend trying different values of n and checking if the outputs may have a physical relevance : as we will see in Section 4.2, the GMCA does not produce images of spurious structures. In theory, the number of components n could be estimated along

with the mixing matrix and the sources. This would require penalizing large values for n using information criteria such as the Minimum Description Length (MDL), the Akaike Information Criterion (AIC) or the Bayesian Information Criterion (BIC). In practice, these approaches are hardly applicable to large-scale real-world applications in imaging since they further necessitate the estimation of an extra discrete variable. This dramatically increases the computational cost without guaranteeing the quality of the separation.

The outputs of the GMCA are an array of dimension (n_E, n) containing the spectral information of the components, and an array of dimension (n, n_x, n_y) containing the spatial information of the components. In order to obtain n normalized cubes of dimension (E, x, y) we multiply each spectrum by its associated image. By collapsing these cubes along the E axis, images of the retrieved sources can be obtained, and by collapsing them along the x and y axis we can obtain their spectra. The spectra can subsequently be used in Xspec or a similar analysis tool in order to fit physical models and retrieve physical parameters (see Section 4.3).

4. Method performance

4.1. Toy model Definition

To test the performance of the GMCA in disentangling components in X-ray data, we designed toy models inspired by real X-ray observations of SNRs. We chose to simulate a SNR similar to Cassiopeia A, one of the best-studied SNR, that has benefited from deep Megasecond observations.

Our toy models consist of a data cube composed of the sum of individual components to which we add Poisson noise. Each component comprises an image multiplied by a spectrum (see Figure 1). The images were obtained by applying the GMCA to real *Chandra* data from Cassiopeia A (see Section 8), and smoothing the output to mitigate the noise. For now, the relevance of these images is not important: we only want to ascertain if, when the components are known, the GMCA is able to disentangle them when mixed together. The spectra we use are the theoretical spectra folded through the *Chandra* instrument response; the energy binning is 43.8 eV (three times the native energy channel width), and the pixel size is 1.8 arcsec (four times the native pixel size). We also add a completely flat image associated with the instrumental background² to better simulate observed data. We do not add a cosmic X-ray background, because this background being isotropic at the scale of CasA, its spatial template would be a flat image. Thus the addition of a cosmic X-ray background and the instrumental background would only end up being one component, with a slightly different spectrum. Finally, we generate Poisson noise. In this study we begin by focusing on two typical observational scenarios (see Table 1): synchrotron continuum emission entangled with line emission (Model 1), and synchrotron continuum emission entangled with thermal emission (Model 2). In both models, we set the synchrotron emission as one with the highest total number of counts.

The results of our method depend on the relative level of the Poisson noise, hence of the total number of counts in the signal. This parameter is thus chosen in order to reflect the reality of the data we get from spectro-imaging instruments. Hence we set the count rate of the synchrotron and line or thermal emission to be of the order of that observed in Cassiopeia A. We then simulated

Table 1: Description of the toy models. For all models, N_{H} is set to $N_{\text{H}} = 0.5 \times 10^{22} \text{ cm}^{-2}$. For the thermal model (*apec*), the ionization timescale is set to $\tau = 1 \times 10^{10} \text{ cm}^{-3} \text{ s}$ and the abundances to solar values.

	Description	Parameters
Model 1	Power Law + Gaussian	$\Gamma = 2.0$ $E_c = 6.58 \text{ keV}$ $\sigma = 80 \text{ eV}$
Model 2	Power Law + Apec	$\Gamma = 2.0$ $kT = 2 \text{ keV}$
Model 3	Power Law + Two Gaussians	$\Gamma = 2.0$ $E_{c1} = 6.55 \text{ keV}$ $E_{c2} = 6.64 \text{ keV}$ $\sigma = 0 \text{ eV}$
Model 4	Power Law + Two Apecs	$\Gamma = 2.0$ $kT_1 = 2 \text{ keV}$ $kT_2 = 0.5 \text{ keV}$

Table 2: Equivalence between the ratios Max(Fe or Thermal emission)/Synchrotron and the physically more significant flux ratios for our four toy models. The components are named after their main characteristic (E_c for the gaussians, kT for the thermal emissions), as they are listed in Table 1. The energy ranges listed below each component are those on which the ratios are calculated.

Models	Model 1	Model 2	Model 3	Model 4
Comp.	E_c	kT	E_{c1}	kT_2
Ratios	6.2 - 7 keV	0.5 - 8 keV	6.4 - 7 keV	0.5 - 4 keV
13.35	4.20	2.39	4.36	1.67
8.90	2.80	1.59	2.91	1.11
5.93	1.86	1.06	1.93	0.74
3.95	1.24	0.71	1.29	0.50
2.64	0.83	0.47	0.86	0.33
1.76	0.55	0.31	0.57	0.22
1.17	0.37	0.21	0.38	0.15
0.78	0.25	0.14	0.26	0.098
0.52	0.16	0.093	0.17	0.065
0.35	0.11	0.062	0.11	0.043
0.23	0.073	0.041	0.076	0.029
0.15	0.049	0.028	0.050	0.019
0.10	0.032	0.018	0.033	0.013
0.069	0.0022	0.012	0.022	0.0086
0.046	0.0014	0.0082	0.015	0.0057

two datasets, corresponding to a 1 Ms or a 100 ks observation with the *Chandra* ACIS-S instrument.

The ratio between the strength of the main component compared to that of the secondary components is also an essential factor. For Model 1, we define this as the Fe Line/Synchrotron ratio at 6.58 keV (the peak of the Gaussian); for Model 2, it is defined as the Thermal emission/Synchrotron ratio at 0.85 keV. We progressively decrease the contrast of the second component relative to that of the synchrotron emission following 15 ratios.

For both toy models we tested the same ratios. Table 2 presents a conversion table between these ratios and the Fe Line/Synchrotron flux ratios between 6.2 and 7 keV, or the Thermal emission/Synchrotron ratio in the 0.5 – 8 keV band.

² Derived from closed/stowed observations available at: <http://cxc.harvard.edu/ciao/download/caldb.html>

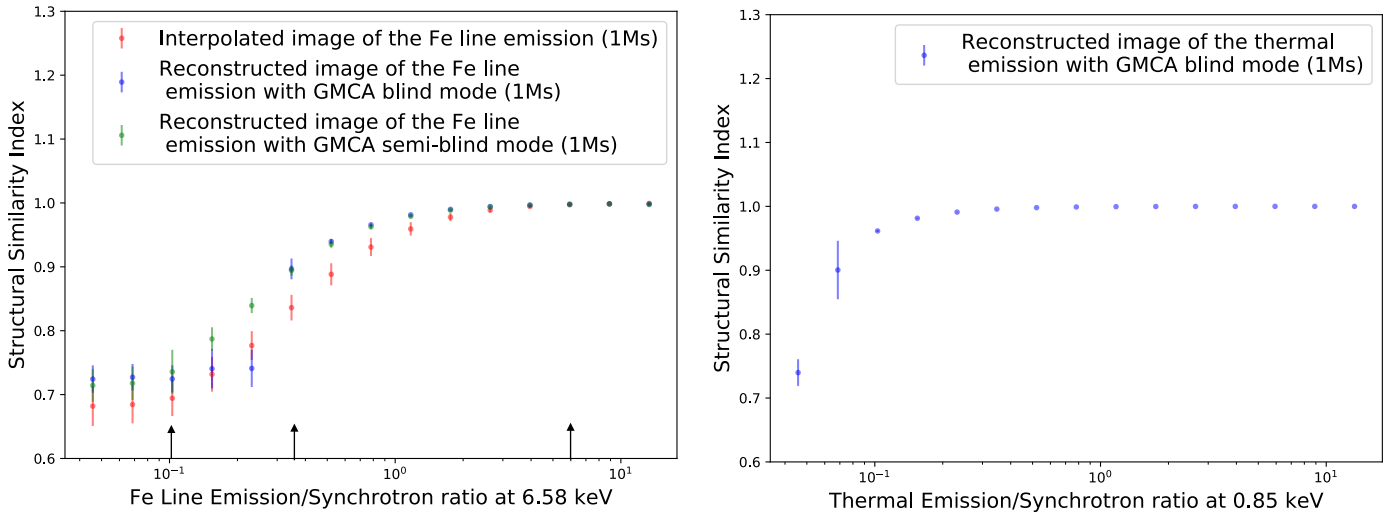


Fig. 2: SSIM coefficients of the input and output images found by GMCA for a total number of counts corresponding to a 1 Ms observation. The points are the average of all Monte-Carlo realizations at a particular ratio, and the error bars the standard deviation of those realizations. On the left, a comparison of the image quality obtained in retrieving the Fe structure in our first toy model for different ratios Line emission/Synchrotron, between an interpolation method, a GMCA in blind mode and a GMCA in semi-blind mode. Some images corresponding to the ratios indicated by arrows are shown in Figure B.1 On the right, the image quality of the thermal emission structure retrieved for different ratios by a GMCA in blind mode.

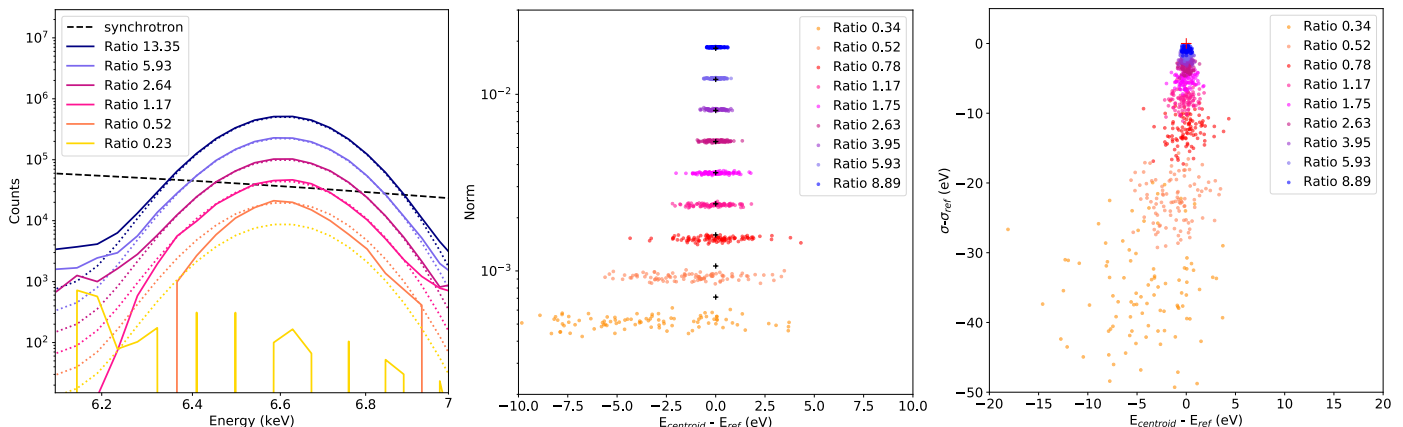


Fig. 3: On the left, spectra retrieved by GMCA for different ratios Fe Line/Synchrotron in our first toy model with a total number of counts corresponding to a 1 Ms observation. In solid lines, the retrieved spectra. In dotted lines, the theoretical spectra. The synchrotron spectrum is displayed as an indication of the relative strengths. The two other plots represent parameters of the Fe K component retrieved by GMCA for a hundred realizations of each out of nine different ratios Fe Line/Synchrotron with a total number of counts corresponding to a 1 Ms observation. In the center, the retrieved E_c and norm. On the right, the retrieved E_c and σ . In both cases, the theoretical results are represented by crosses.

296 4.2. Reconstructed image fidelity

297 To assess the accuracy of the results of the GMCA, we compared
298 both the similarities between the input and the output images,
299 and the reliability of the spectral parameters fitted. For the im-
300 age benchmarks, we used the Structural Similarity Index (SSIM,
301 see Wang et al. 2004), which measures the perceived simi-
302 larities between two images by incorporating perceptual phenomena
303 and the idea that close pixels have strong inter-dependencies, in-
304 stead of solely measuring absolute differences. This index takes
305 the form of a number between 0 and 1, 1 being a perfect resem-
306 blance and 0 indicating perfect dissimilarity. In our case, below
307 an SSIM of 0.75 we can consider that the source has not been
308 retrieved, the remaining correlations being linked to the simi-

larities between the synchrotron image, the Fe image and the Poisson noise associated to them. 309
310

For each line/continuum emission ratio we then performed 311 a Monte-Carlo simulation of a hundred different Poisson real- 312 izations to test the robustness of the algorithm. We compared 313 the results of the GMCA in pure blind mode with that of the 314 GMCA in semi-blind mode, with the theoretical shape of the Fe 315 line fixed. We also compared these results to that of an inter- 316 polation method between 6.1 and 7.1 keV (Figures 2, left panel 317 and B.2, left panel show the results for the simulated 1Ms and 318 100 ks observations, respectively). This method consists of es- 319 timating the underlying synchrotron spectrum between 6.1 and 320 7.1 keV by interpolating it. The synchrotron image is then deter- 321

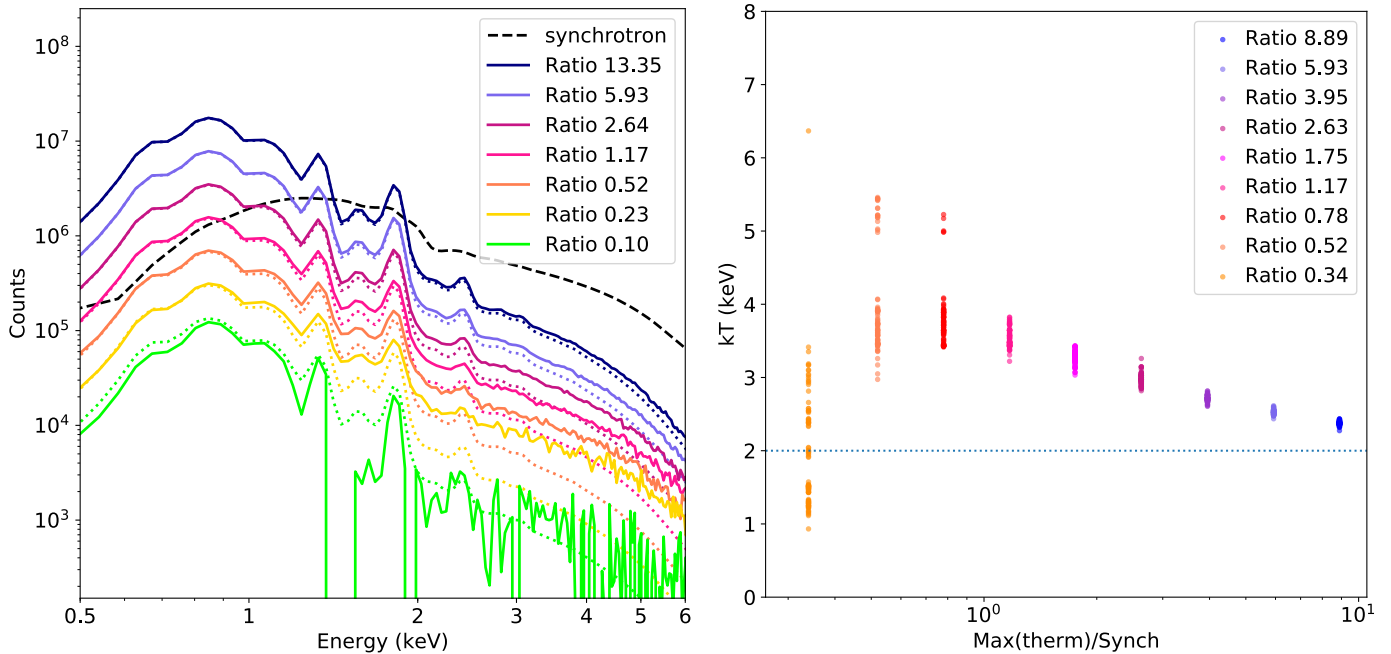


Fig. 4: On the left, spectra retrieved by GMCA for different ratios Thermal emission/Synchrotron with a total number of counts corresponding to a 1 Ms observation. In solid lines, the retrieved spectra. In dotted lines, the theoretical spectra. The synchrotron spectrum is displayed as an indication of the relative strengths. On the right, kT retrieved by Xspec by fitting a thermal model on the thermal emission spectra retrieved by GMCA for different ratios Fe Line/Synchrotron with a total number of counts corresponding to a 100 ks observation. For each ratios, we made a Monte-Carlo with a hundred realization, fitting in Xspec a thermal model on every realization associated with the error bars given by the Monte-Carlo. The theoretical kT is 2 keV and is indicated by the blue dotted line.

322 mined by integration (for example between 5 and 6 keV, where
323 the Fe is absent) and the synchrotron cube is obtained by multi-
324 pling this image and the interpolated spectrum. Then, we sub-
325 tract the aforementioned cube synchrotron-subtracted remaining
326 cube constitutes an estimation of the Fe structure.

327 For both simulated exposures, we see that Fe
328 Line/Synchrotron ratios images given by the GMCA have
329 slightly better SSIM coefficients to those obtained with an
330 interpolation method. However, a sudden drop in the GMCA
331 results points out the moment when the algorithm in blind
332 mode is no longer able to find the Fe structures. The descent
333 is smoother with a fixed spectrum (semi-blind mode) because
334 the algorithm is given more information to search for potential
335 sources, but as the number of counts in the iron line decreases
336 the noise increases. In blind mode, the GMCA retrieves an
337 image of the Fe spatial structure when it is up to 2.9 times
338 weaker than the synchrotron in the case of a total number of
339 counts corresponding to a 1 Ms observation (9 times weaker in
340 flux), and up to 1.8 times higher than the synchrotron for 100 ks
341 (1.8 times weaker in flux).

342 The GMCA in blind mode does not benefit from the infor-
343 mation that the Fe line is contained between 6.1 and 7.1 keV, still
344 gives great results. Furthermore, the interpolation method cannot
345 be used on components whose spectra are extended on an energy
346 range that is too wide, as we will see with our second toy model.
347 Also, we will see in Section 8 that with real data, what looks like
348 a Gaussian can contain some hidden information that a GMCA
349 in blind mode will be able to retrieve, but an interpolation can
350 only find the Gaussian as a whole.

351 The fact that the GMCA gives good images until it is sud-
352 denly unable to find anything but noise suggests that the algo-
353 rithm can be trusted : in this particular test the Fe distribution is

354 found or is not, but the algorithm never gives images of spurious,
355 over-interpreted structures (see B.1 for an example of images be-
356 coming noisier as the component becomes fainter). In our test
357 case, when we increase the number of sources, the first two re-
358 main the synchrotron and Fe structure, the rest are only noise. As
359 our data are Poissonian, the noise component has a shape similar
360 to that of the main component, here the synchrotron, with large
361 fluctuations.

362 We proceeded in the same way with our second toy model,
363 featuring a synchrotron continuum emission and a thermal emis-
364 sion (see Figure 2, right panel for the simulated 1Ms observation
365 and Figure B.2, right panel for the 100 ks one). Here, the compar-
366 ison with an interpolation method is impossible, for the thermal
367 spectrum cannot be subtracted from the synchrotron with a sim-
368 ple interpolation. The GMCA in semi-blind mode does not make
369 sense either, for with real data it would be impossible to know
370 the shape of a thermal emission a priori. With a total number of
371 counts corresponding to a 1 Ms observation, the GMCA in blind
372 mode applied from 0.5 to 10 keV is able to retrieve an image of
373 the thermal emission spatial structure when this component is up
374 to 14.6 times weaker than the synchrotron (83.3 times weaker in
375 flux). With a total number of counts corresponding to a 100 ks
376 observation, it could retrieve an image up to 4.3 times weaker
377 than the synchrotron (13.7 times weaker in flux). The thermal
378 emission in our second toy model can be retrieved with smaller
379 ratios than the Fe line because it is non-negligible on a wider
380 energy range, providing more counts to the algorithm.

381 We can note that the instrumental background was not re-
382 trieval, in any cases, and that it did not leak on any other com-
383 ponent. This is due to the fact that the two largest wavelet scales
384 being eliminated, the instrumental background, associated with
385 a flat image, was automatically suppressed with it.

386	4.3. Spectral fidelity	3.95 we retrieve $(9.13 \pm 0.05) \times 10^9 \text{ cm}^{-3} \text{ s}$, and for a ratio of 448 0.34, $(9.12 \pm 0.27) \times 10^9 \text{ cm}^{-3} \text{ s}$. 449
387	For every Fe Line/Synchrotron ratio for which the Fe K distribution is found by the GMCA in blind mode, the retrieved spectrum is comparable to the input spectrum with some noise appearing as the Fe component becomes fainter (see Figure 3, left panel). Apart from a slight overestimation of the wings, the retrieved spectra are accurate and their normalizations well estimated.	
388		
389		
390		
391		
392		
393	In order to estimate more precisely the spectral accuracy of the method, we fitted the recovered spectra in Xspec and compared the parameters thus obtained with a fit of the original data without GMCA processing directly in Xspec. Fitting the retrieved spectra requires to estimate the errors for every spectral bin. In spite of the fact that our input data are Poissonian, we cannot assume that the results given by the GMCA will still be such. Therefore, we used the standard deviation of a hundred Monte-Carlo realizations as an estimation of the error.	
394		
395		
396		
397		
398		
399		
400		
401		
402	We tested the accuracy of the spectra retrieved by the GMCA in Model 1 by comparing their centroids, widths and normalizations to the theoretical ones (see Figure 3, central and right panels). The norms are almost perfectly retrieved (Figure 3, left and central panels), and even the slight energy shift for the smaller ones (around 5 eV) is negligible as compared to the instrument resolution, which is 150 eV (at 5.9 keV) for the ACIS-S camera ³ . The wings are a little overestimated in the first norms (Figure 3, left panel), while the width σ is underestimated in the last ones (Figure 3, left and right panels). It may be due to the fact that in the fainter part of the Gaussian, the signal is largely dominated by the synchrotron, which makes the disentanglement harder than at the peak of the Gaussian.	
403		
404		
405		
406		
407		
408		
409		
410		
411		
412		
413		
414		
415	We made the same comparison with the Gaussians recovered without using GMCA by fitting a power law and a Gaussian on the original spectra in Xspec (see Figure B.3). The retrieved norms and centroids are a little more accurate (Figure B.3, left panel), but quite similar to the results given after GMCA. However, the retrieved σ are not underestimated, they are still centered on the theoretical value for low ratios (Figure B.3, right panel). Thus, the GMCA introduces a bias in calculating some physical parameters in Xspec, but it is minimal compared to the 150 eV spectral resolution.	
416		
417		
418		
419		
420		
421		
422		
423		
424		
425	Finally, we tested the accuracy of the spectra retrieved by GMCA in our second toy model, featuring a synchrotron and a thermal emission (see Figure 4, left panel). The spectra are mainly well retrieved, even for low thermal emission/synchrotron ratios, but they are always overestimated at high energies. That reflects the fact that the synchrotron is contaminating the thermal emission : because of the spatial overlap between the two structures, there is a leakage from the main one into the weaker one when the number of counts is too low. This leakage impacts strongly the temperature retrieved after a fitting in Xspec, the necessary information being the slope at high energies. As shown in Figure 4, right panel, the overestimation of the spectra, bigger as the ratio decreases, is directly affecting the retrieved kT . However, kT is a global parameter, relying on the information contained over the full energy range, thus highly susceptible to be impacted by an overestimation at high energies. Local parameters, like N_{H} or τ , are almost perfectly estimated for thermal/synchrotron ratios as low as 0.52. For example, the theoretical N_{H} is equal to $0.5 \times 10^{22} \text{ cm}^{-2}$, and for a ratio of 3.95 we retrieve $(0.490 \pm 0.001) \times 10^{22} \text{ cm}^{-2}$ and for a ratio of 0.34, $(0.485 \pm 0.008) \times 10^{22} \text{ cm}^{-2}$ where errors are the standard deviation on a hundred Monte-Carlo realizations. In the same way, the theoretical τ is $1 \times 10^{10} \text{ cm}^{-3} \text{ s}$; for a ratio of	
426		
427		
428		
429		
430		
431		
432		
433		
434		
435		
436		
437		
438		
439		
440		
441		
442		
443		
444		
445		
446		
447		
5. Implementing a new inpainting step in the GMCA 450		
In this section we will discuss the introduction of an extra step 451 in the GMCA algorithm based on an inpainting method. Inpaint- 452 ing is a process consisting in reconstructing parts of an image 453 that are lost or willingly removed. In photography, it can be 454 used to clean the image, remove defaults or inappropriate details. 455 This tool proved useful to improve our blind source separation 456 method. 457		
We previously saw that in the results given by the GMCA 458 on toy models composed of two physical sources there could be 459 some leakage from the main component to the other one (e.g. 460 leakage of the synchrotron component to the thermal component 461 in Fig. 4). These leakages are often balanced by negative parts 462 in the main component's image or spectrum. In order to correct 463 that leakage, we added an extra step to the GMCA. 464		
The GMCA being an iterative algorithm, our revised version 465 retains a loop of about 150 iterations of the usual algorithm, fol- 466 lowed by a smaller loop with a new step in which each result of 467 the previous state is treated in a way to forbid negative values. To 468 do so, a first method would be to define a mask where the recon- 469 structed images take negative values, and apply those masks to 470 the wavelet transforms of those images, S , imposing a 0 value on 471 the negative parts before they are processed to estimate A . The 472 results can be improved by replacing the raw masking by an in- 473 painting, here a reconstruction of the masked parts of the image 474 using a wavelet transform (see Fadili et al. 2007). We do this in 475 order to constrain the algorithm to converge to a more physical 476 solution. 477		
Our new loop can be described thus : 478		
– Step 1 : Estimation of S thanks to X and the previous A . 479		
– Step 2 : Defining masks set to 0 where the reconstructed im- 480 ages are negative, indicating an area where strongly corre- 481 lated components are overlapping, and 1 elsewhere. 482		
– Step 3 : Inpainting of S (in wavelets) using the masks previ- 483 ously defined. 484		
– Step 4 : Estimation of A for fixed S by minimizing $\ X - AS\ _F$. 485		
As can be seen in Figure 6, our inpainting step corrects well 486 the leakage from the synchrotron to the thermal emission compo- 487 nent in our second toy model : the retrieved spectra are closer to 488 the truth. The resulting impact on the fitting in Xspec is also sig- 489 nificant, as the temperatures are now more accurately retrieved 490 for sufficiently high Thermal emission/Synchrotron ratios (see 491 Figure 6). The convergence of our new loop is not mathemati- 492 cally proven, but we empirically noted that the solution stabi- 493 lized quickly. In the science cases that we have explored, three 494 iterations were sufficient to recover more accurate spectral re- 495 sults. 496		
6. Estimating errors with only one realization 497		
The Monte-Carlo method cannot be used to retrieve error bars 498 with real data, as only one observation is available : the observed 499 one. Thus, a resampling method such as the Bootstrap (see Efron 500 1979), able to simulate several realizations out of a single one, is 501 necessary. 502		

³ <http://cxc.harvard.edu/cal/Acis/>

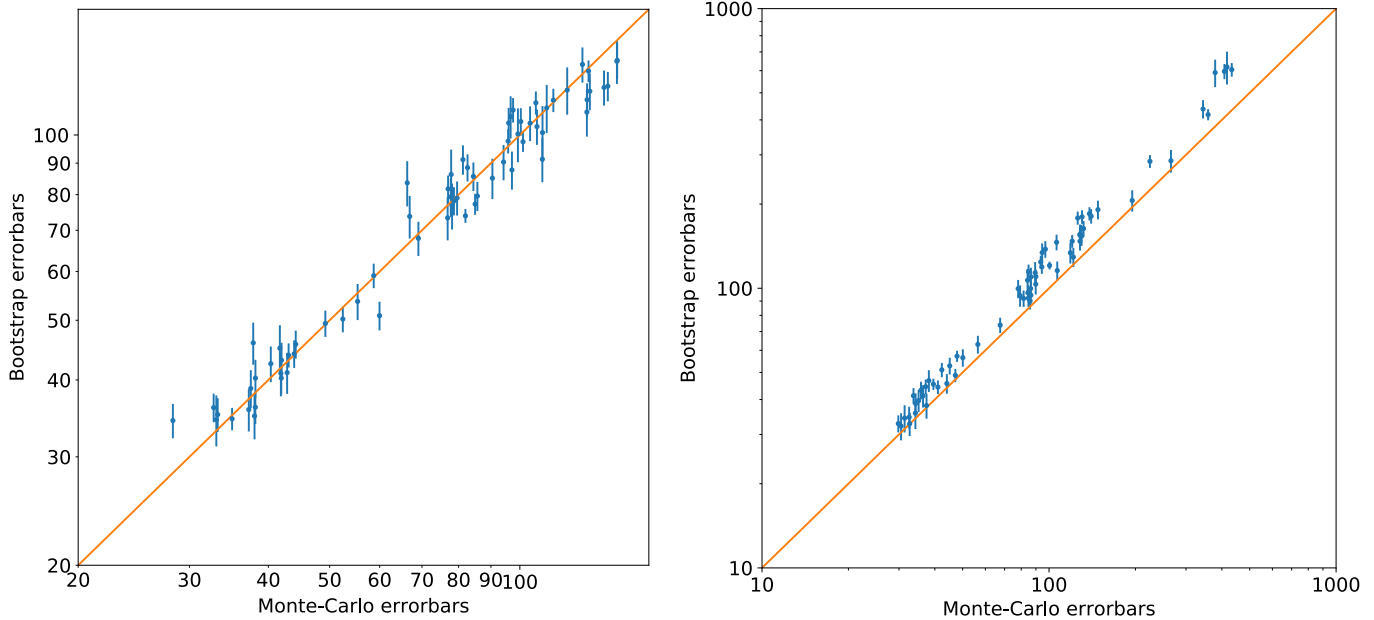


Fig. 5: Correlation between the error bars given by the standard deviation of a hundred Monte-Carlo and the error bars given by the standard deviation of a hundred simulated realizations resampled out of a single one thanks to the Block Bootstrap method, with and without GMCA. On the left, the spectra are those of the Fe gaussian in our first toy model with a total number of counts corresponding to a 100 ks observation and a line/continuum ratio of 5.93 (in the absence of a synchrotron spectrum, this ratio characterizes the gaussian's norm. 5.93 corresponds to the fourth norm in our previous tests). On the right, we compare Monte-Carlo and Block Bootstrap error bars on the results given by GMCA on our first toy model, for the same duration and ratio. In both cases, we made a hundred Monte-Carlo realizations and we used a Block Bootstrap resampling on ten realizations, a hundred times each, for a block length of 78 (cube root of the total number of events) in order to evaluate the influence of the initial realization on a Block Bootstrap resampling

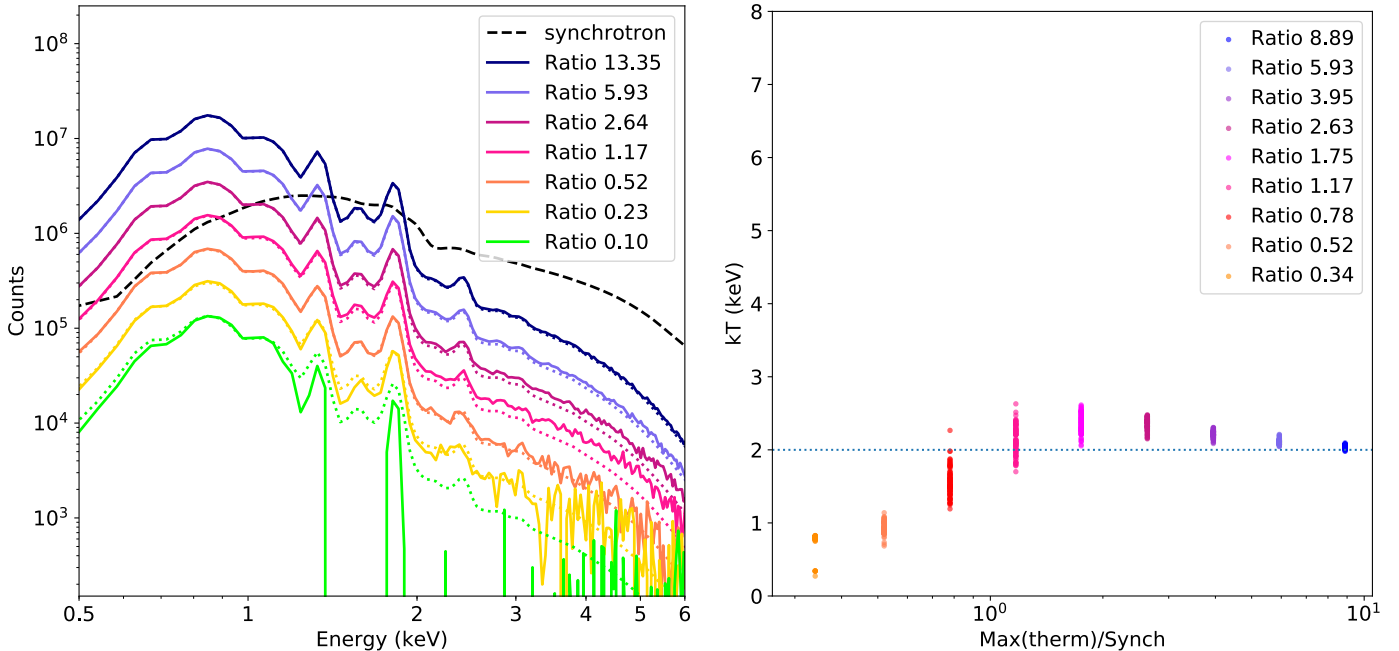


Fig. 6: Same as Figure 4 after the inpainting step described in Section 5.

503 6.1. Block Bootstrap

504 The Bootstrap is a statistical method consisting of a random sam-
505 pling with replacement from a current set of data. If the initial

506 data is a collection of N events, a resampling obtained through
507 bootstrapping would be a set of N events taken randomly with
508 replacement amid the initial ones. This method can be repeated

509 in order to simulate as many realizations as needed to estimate
 510 standard errors or confidence intervals. In order to save calcula-
 511 tion time, we choose to resample blocks of data of a fixed size
 512 instead of single events : this method is named Block Bootstrap.
 513

514 In our case, the data is the set of all photons detected by an
 515 X-ray telescope during its observation time, each photon being
 516 considered as a triplet (E, x, y) . Because of the massive amount
 517 of events, we use a block bootstrap resampling method. The
 518 ordering variable is time, independent of (E, x, y) , so defining
 519 blocks preserves the random character. There is no proper way
 520 to choose a block length a priori; a few tests seem to indicate that
 521 a length of the order of the cube root of the total data set size is
 522 efficient with our type of data.

523 The errors on the spectra are calculated as the standard devi-
 524 ation of the values on each energy bin over all new samples. The
 525 error on the i-th bin is thus :

$$\text{error}[i] = \sqrt{\frac{\sum_{j=1}^n (\text{spec}[i, j] - \overline{\text{spec}[i]})^2}{n}} \quad (3)$$

525 Where n is the number of resamples, $\text{spec}[i, j]$ the value of
 526 the spectrum in the i-th bin of the j-th sample and $\overline{\text{spec}[i]}$ the
 527 mean of the values of the spectra in the i-th bin over the n resam-
 528 ples.

529 6.2. Estimated Errors

530 Our aim in using a Block Bootstrap resampling method is to es-
 531 timate errors on the spectral data points that will allow us to fit
 532 spectra issued from real data in **Xspec**. In the first place, we com-
 533 pared the error bars given by a hundred Monte-Carlo realizations
 534 of the Fe Gaussian alone to those retrieved by these methods out
 535 of a single one. The data we used was the Fe Gaussian of our
 536 first toy model between 5 and 8 keV for a 100 ks observation
 537 and a ratio of 5.93.

538 To do so, for every energy bin we looked at the correlation
 539 between the standard deviation of the spectral values as given
 540 by a Monte-Carlo and by the Block Bootstrap method; and by
 541 applying the resampling method to different realizations we were
 542 able to evaluate the errors on the Bootstrap error bars (i.e. the
 543 uncertainty induced by using one given observation). In Figure
 544 5, we see that the error bars obtained through resampling are
 545 consistent with the Monte-Carlo error bars.

546 To know if applying the GMCA algorithm introduces a bias,
 547 we also compared the error bars given by the standard deviation
 548 of a hundred GMCA applied on different Monte-Carlo realiza-
 549 tions and that given by a hundred GMCA applied on a hundred
 550 resamples.

551 The error bars obtained through GMCA applied on a hun-
 552 dred Block Bootstrap resamplings are slightly overestimated in
 553 comparison with those obtained with Monte-Carlo, but it does
 554 not have a crucial impact on the best-fit parameters obtained in
 555 **Xspec** (see Figure 7).

556 7. GMCA applied on toy models with more than two 557 components

558 We designed two more toy models featuring three sources in-
 559 stead of two (see Table 1, and Table 2 for flux ratios). In our
 560 third toy model, we put a synchrotron and two Gaussians cen-
 561 tered respectively on 6.54 keV and 6.63 keV. The one at 6.63

keV has a norm equal to 0.7 times that of the other one. Here, 562 the Gaussians are the instrumental responses to a Dirac, hence 563 they have a smaller width than in the first toy model. This is 564 what we would get if the first wide Gaussian truly was the sum 565 of two thinner ones slightly shifted. As we need a more precise 566 definition in energy, the binning is thinner than in our previous 567 toy models (14.6 eV), but the total number of counts are of the 568 same order. 569

570 In our fourth toy model, we put a synchrotron and two ther-
 571 mal emissions, one with kT equal to 0.5 keV, the other with kT
 572 equal to 2 keV. The norm of the first one is equal to 0.7 times
 573 that of the second one. For the images, we used the blue and
 574 red shifted Fe components shown in Figure 9. As for our first
 575 two toy models, we added to our third and fourth toy models a
 576 flat image associated with the spectrum of an instrumental noise,
 577 and we generated Poisson noise on the whole data cube. The to-
 578 tal number of counts of the synchrotron corresponds to a 100
 579 ks observation, and the second main component (the brightest
 580 Gaussian or thermal emission)/synchrotron ratios we tested are
 581 the same as before.

582 The GMCA is able to disentangle properly the three sources
 583 for the highest second main component/continuum ratios, but
 584 when the sources weaken, it only retrieves the synchrotron and a
 585 second source that is a composite of the two Gaussians, or of the
 586 two thermal emissions. Using the inpainting step helps disentan-
 587 gling the three sources a little longer and improves the spectra
 588 in the thermal emission case, but the weakest thermal emission
 589 is underestimated : the leakage mechanism is more difficult to
 590 correct with three sources to disentangle than with only two of
 591 them. In Figure 7, we can see an example of correct disentan-
 592 glement of the components in both toy models. The presented
 593 line/continuum and thermal/continuum ratios are the last ones to
 594 give correct images and correct spectra for every component.

595 We fitted the retrieved thermal emission spectra of our fourth
 596 toy model in **Xspec**, in order to estimate kT . We first used as er-
 597 rror bars the standard deviation of a hundred MC realizations;
 598 then, we took the standard deviation of a hundred Block Boot-
 599 strap resamplings of a single MC realization. The first thermal
 600 emission's temperature is slightly overestimated with MC error
 601 bars, but the overestimation is of the same order as with our
 602 second toy model. However, it is consistently retrieved with the
 603 Block Bootstrap error bars. The second thermal emission's tem-
 604 perature is slightly underestimated in both cases.

605 8. GMCA applied to real data

606 Following the consistency and the robustness tests described
 607 above, we applied the GMCA to the deep *Chandra* observations
 608 of Cassiopeia A, which was observed with the ACIS-S instru-
 609 ment in 2004 for a total of 980 ks (ObsID : 4634, 4635, 4636,
 610 4637, 4638, 4639, 5196, 5319, 5320). The spectrum from the
 611 whole SNR, together with the main emission features, are shown
 612 in Figure 8. The event lists from all observations were merged in
 613 a single data cube. For each application described in the sec-
 614 tions below, the spatial and spectral binning were adapted so as
 615 to obtain a sufficient number of counts in each cube element.
 616 No background subtraction or vignetting correction has been ap-
 617 plied to the data. We note that due to the lack of exposure and
 618 background map handling with the current version of GMCA,
 619 the method can not yet be applied to large mosaic of observa-
 620 tions.

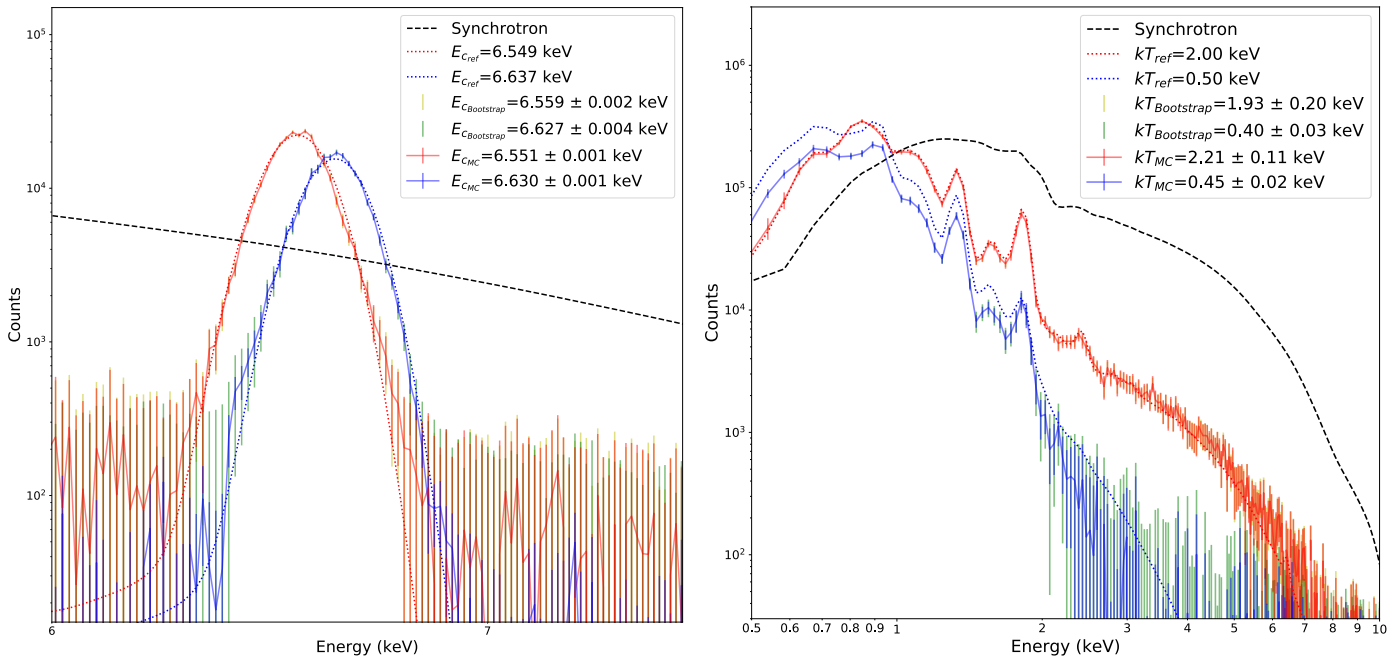


Fig. 7: Spectra retrieved by GMCA in our third and fourth toy models with a total number of counts corresponding to a 100 ks observation. On the left, spectra retrieved by a GMCA with inpainting step of the two gaussians in our toy model 3, with a First line emission/Continuum ratio of 5.93 and a thinner binning (14.6 eV). On the right, the spectra retrieved with an inpainting step of the two thermal emissions in our toy model 4, with a First thermal emission/Continuum ratio of 2.64. To compare both error estimation methods, we added the error bars and the kT given by a hundred MC realizations, and those given by a hundred Block Bootstraps resamplings of a single MC realization.

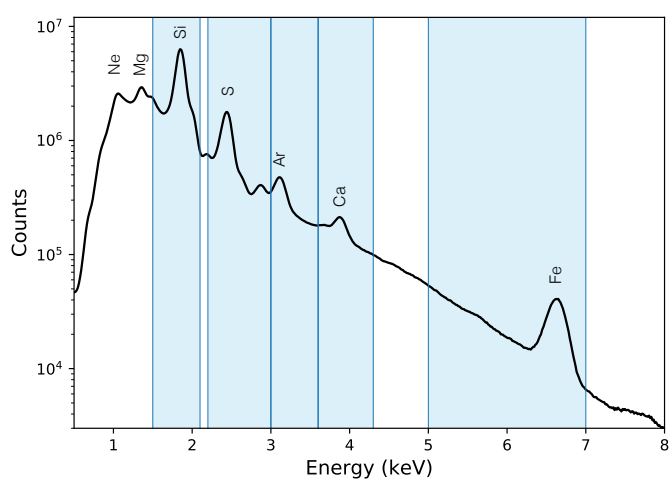


Fig. 8: Spectra of Cassiopeia A from the deep 2004 observations. The main emission lines are labeled as well as the energy ranges used for the GMCA algorithm in Figure 10.

621 8.1. Asymmetries of the Fe K distribution in Cassiopeia A

622 We first applied the GMCA to the Cassiopeia A observation be-
 623 tween 5 keV and 8 keV, where the prominent features are known
 624 to be the synchrotron emission and the Fe K line complex. To
 625 allow for unexpected sources to be retrieved by the algorithm,
 626 it is recommended to decompose the data into a larger number
 627 of components than expected as a first guess. By doing this, we
 628 obtained three physically meaningful components in Cassiopeia
 629 A: continuum emission, and two Gaussian lines that appear to

be slightly shifted with respect to one another, and from the Fe K average energy. The first component is undoubtedly the synchrotron emission, for which the image is coherent with our knowledge of its spatial distribution; the corresponding spectrum can be described as a power law (Figure 9, top panel). The two other components have spectra corresponding to blue/red shifted Fe line emission (Figure 9, middle panels), and the associated images show clumps typical of the spatial distribution of Fe in Cassiopeia A (see DeLaney et al. 2010, Figure 7). If we instead require the algorithm to find only two components, it retrieves the synchrotron emission and a composite of the two Fe components. If we impose on the algorithm to find more than three components, the additional retrieved sources are simply noise . The bottom panel of Figure 9 shows an image of what we identify as noise in such a case.

The block bootstrap resampling step outlined in Sect. 6.1 allowed us to extract the spectra corresponding to the different components above. Fitting the Fe K line emission in Xspec with a Gaussian model, the red-shifted part was found to peak at 6.726 ± 0.002 keV, and the blue-shifted part peaks at 6.561 ± 0.001 keV . These energies suggest a relative velocity between the red and blue-shifted components of 7440 km s^{-1} , a value that is coherent with the results shown in Fig. 7 of DeLaney et al. (2010).

Our method allows direct imaging of the red- and blue-shifted Fe K components with unprecedented spatial resolution. In addition, instead of estimating a mean shift in each line of sight (such as would be obtained when fitting with one Gaussian is performed), our method can disentangle the red and blue-shifted components along a line of sight as shown in Fig. 9, where both emissions co-exist in the South-East.

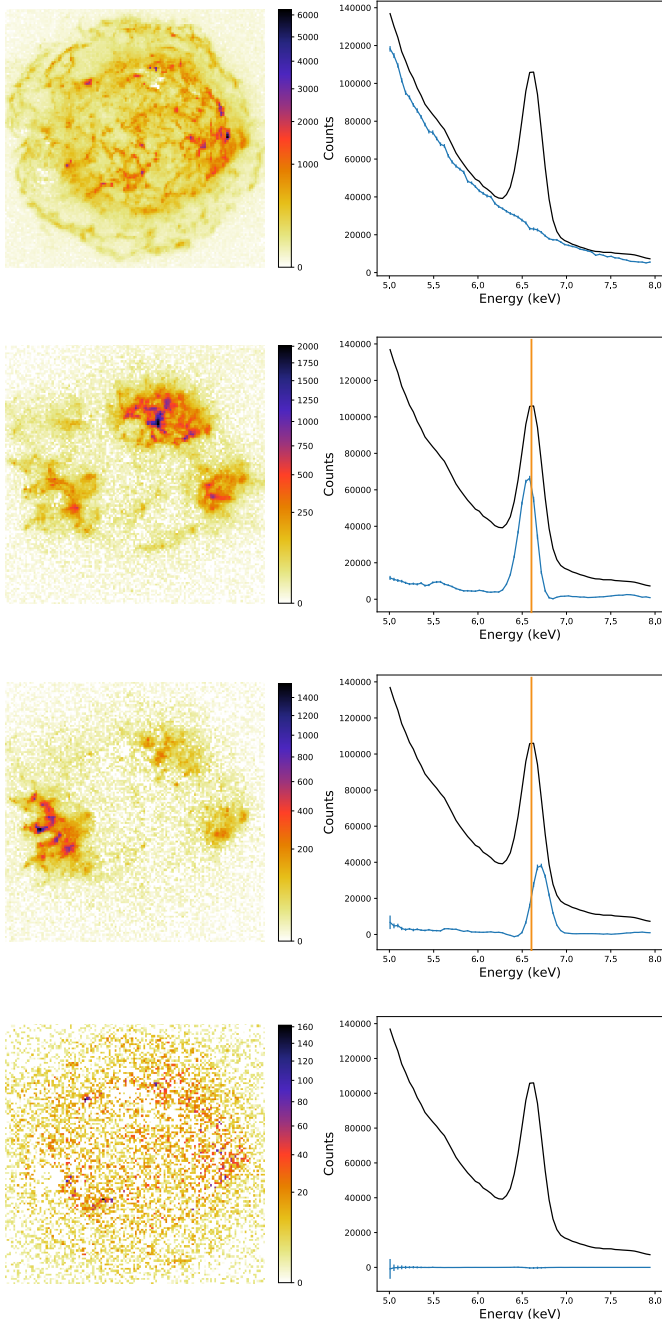


Fig. 9: Images and spectra retrieved by the GMCA with inpainting step in the real data from Cassiopeia A between 5 keV and 8 keV. The first source corresponds to a synchrotron emission, while the two following are parts of the Fe distribution. The first one is a red shifted part of this distribution, while the second one is a blue shifted part of the distribution. The error bars in both parts of the Fe distribution are retrieved thanks to a block bootstrap of length 78. A fitting in Xspec gives the line energies of 6.726 ± 0.002 keV for the blue-shifted part and 6.561 ± 0.001 keV for the red-shifted part. The last image is the one we identify as noise.

8.2. Spatial structures of the main line emissions in Cassiopeia A

Figure 10 shows an application of the method to the main line emission bands in Cassiopia A, centred on Si, S, Ar, Ca, and Fe.

In each case, the GMCA was able to retrieve two images corresponding to a slightly red-shifted and a blue-shifted component. 664
665

We compared the spatial structures of these components to what could be retrieved by an interpolation method (see Section 666
667 4.2) around these same line emissions. As we can see in Figure 668
669 10, both methods give consistent results, although the GMCA 670
671 retrieves more structures for faint lines (Ar and Ca). More 672
673 importantly the GMCA can probe structures within a broad line 674
675 and reveal line shifts, information that cannot be yielded by the 676
677 interpolation method. The blue-shifted and red-shifted images 678
679 are completely independent. 680

8.3. Spatial distribution of continuum components in Cassiopeia A

We applied our method on Cassiopeia A data between 0.6 and 679
680 2.3 keV. The number of counts being higher in this energy band, 681
682 we used data with a finer spectral binning (14.6 eV instead of 43.8 eV) and smaller pixels (0.9 arcsec instead of 1.8 arcsec). 683

Figure 11 shows the four components were retrieved. The 684
685 first corresponds to the synchrotron emission, and is coherent 686
687 with the image we retrieved between 5 and 8 keV. It is the first 688
689 time an image of the synchrotron has been extracted in these 690
691 energy bands, where it is dominated by the ejecta emission. Such a 692
693 map of the low-energy synchrotron emission is very valuable for 694
695 the study of the energy dependence of the synchrotron rim width. 696
697 A second component has a spatial distribution highly similar to 698
699 that of the Fe K between 5 and 8 keV, and the line emission complex 700
701 at ~ 1 keV in the corresponding spectrum seems to indicate 702
703 that this component may be dominated by the Fe L complex. 704

The final two components have spectra corresponding to 694
695 slightly red or blue-shifted Si emission. Their spatial distributions 696
697 are similar: we can thus deduce that both components correspond 698
699 to Si emission, one being slightly red-shifted, and the other slightly blue-shifted. The morphology of the two parts 700
701 are globally consistent with previous works but are endowed 702
703 with more details (see for example Figure 7 of Willingale et al. 704
705 (2002), or DeLaney et al. (2010) for a comparison with optical 706
707 images). We note that each thermal component is not completely 708
709 dominated by a unique line structure. For example, we see that the Si components (Figure 11 right panels) also contain 710
711 Oxygen and Magnesium emission in their spectra. Oxygen and 712
713 Magnesium are grouped together with Si by the algorithm because 714
715 they have similar plasma conditions (temperature, abundances, ionization stage) and spatial distributions. More surprisingly, the component exhibiting Fe L emission (Figure 11 bottom left panel) also has strong Mg XII and Si XIV line emission. This indicates that the Fe L is co-spatial with Mg and Si in a higher ionization state than in the Si dominated components. While the reason of this difference is still unclear, this example shows the power of GMCA to disentangle physical components in complex environments.

9. Discussion and Conclusions

The separation of entangled components in the X-ray data of extended sources is a challenging task. Isolation of the morphology 717
718 and associated spectrum of the individual components could provide 719
720 new insights into the physical and thermodynamical conditions 721
722 of the plasma in these objects. In the case of supernova remnants, those measurements could lead to a better understanding 723

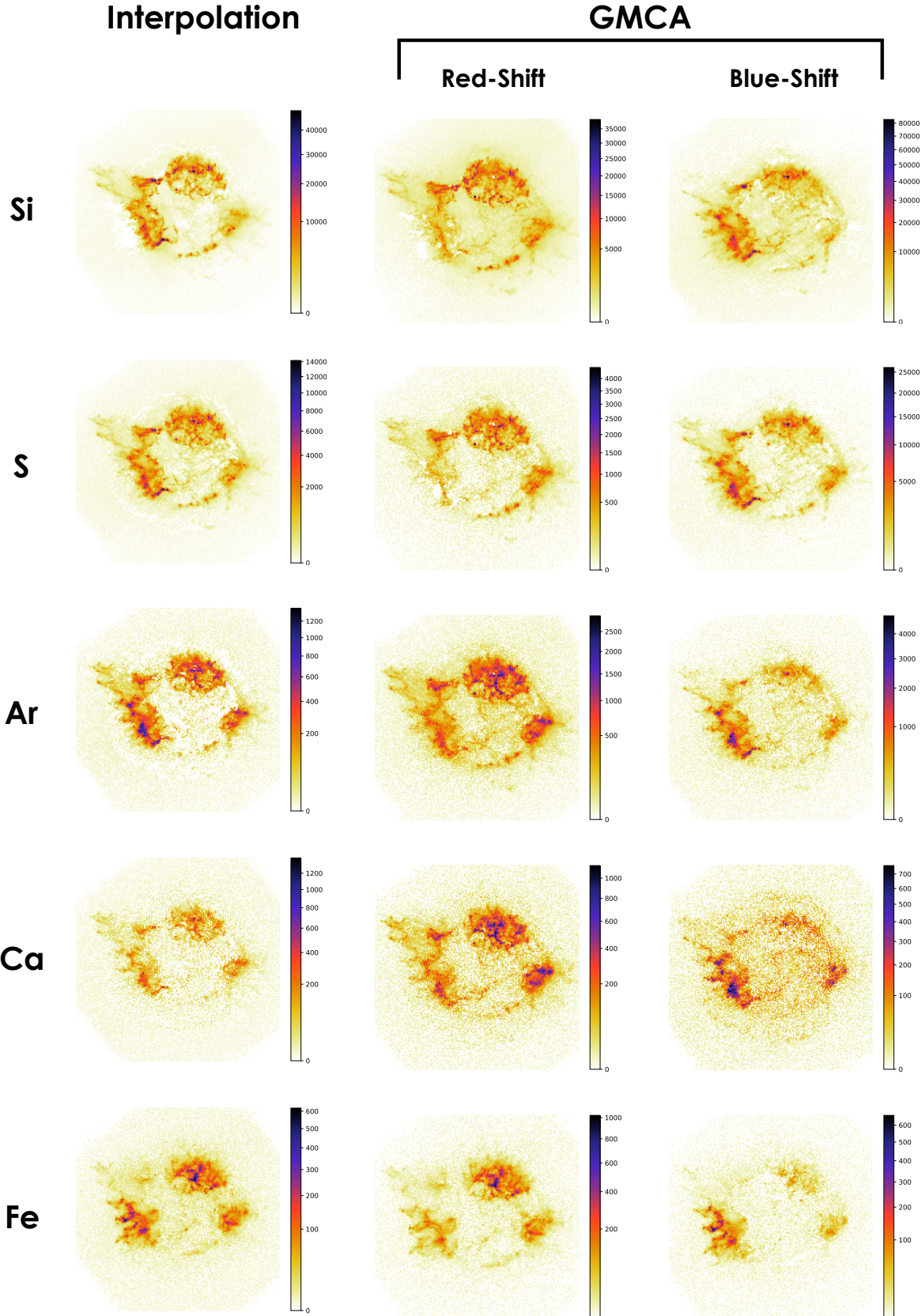


Fig. 10: Images of the spatial structure of the main line emission in Cassiopeia A as retrieved by an interpolation method (left column), and from application of GMCA around the respective line emission region (middle and right columns). In all cases, the GMCA algorithm decomposes the line emission into two images, corresponding to spectra that are slightly red-shifted and slightly blue-shifted with respect to the rest-frame line position. The energy ranges used for GMCA are shown in Figure 8. The energy ranges used for the interpolation method are respectively : 1.7 – 2 keV, 2.25 – 2.6 keV, 3 – 3.35 keV, 3.7 – 4.1 keV and 6.2 – 7.1 keV.

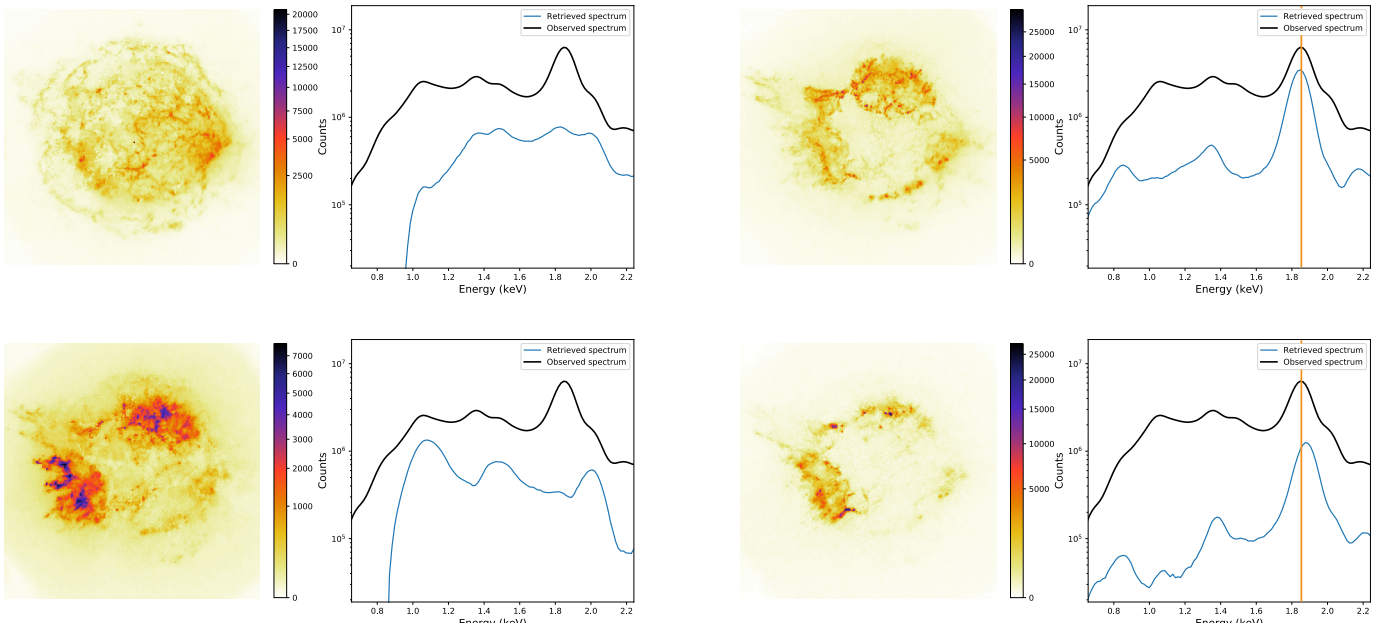


Fig. 11: Images and spectra retrieved by the GMCA with inpainting step in the real data from Cassiopeia A between 0.6 keV and 2.3 keV with a spectral binning of 14.6 eV and pixels of a 0.9 arcsec size. On the upper left, we recognize the synchrotron emission. On the lower left, the retrieved component seems to be dominated by Fe L. On the right, two components dominated respectively by red and blue-shifted Si.

723 of the explosion mechanisms, gas heating and particle acceleration.
724

725 We presented here a method based on the GMCA, a blind
726 source separation algorithm developed to extract the CMB from
727 *Planck* data. The method uses the full information contained in
728 data cubes (E, x, y), and extracts the unique spatial and spectral
729 signatures of the entangled components without any prior informa-
730 tion (neither physical models nor instrument response func-
731 tions). It has been applied here to X-ray data for the first time,
732 and we have shown that it provides better results than the usual
733 methods in use in this field.

734 The GMCA needs to be applied to data with a large total
735 number of counts. When such data are available, it can suc-
736 cessfully disentangle highly spatially correlated sources, as was
737 shown with our toy models (Sections 4 and 7). A first application
738 to real *Chandra* data of Cassiopeia A in different energy bands,
739 detailed in Section 8, gave promising results, highlighting the
740 asymmetries in the Si, S, Ar, Ca and Fe K spatial distributions
741 by retrieving two maps associated to spectra that are slightly red-
742 or blue-shifted with respect to the rest-frame line.

743 The main conclusions of our study are the following:

744 – **Morphological Fidelity:** In every example we tested, it ap-
745 peared that the GMCA yields accurate images of the sources
746 it retrieves, very close to the original ones we injected in the
747 toy model. Furthermore, while the cases we tested were very
748 challenging, the sources being spatially highly entangled, our
749 method succeeded in retrieving detailed disentangled images
750 of each component. Lastly, the algorithm never retrieved any
751 artifact that did not belong to the toy model: when the second
752 component/main component ratio was too weak, the second
753 component was not retrieved, but everything that was could
754 be trusted was a bona-fide component, and not a false detec-
755 tion.

756 – **Spectral Fidelity:** While the initial GMCA retrieves correct
757 images there is a leakage which affects parameters that de-

pend on a wide energy range when the spectra are fitted in **Xspec**. An inpainting step we added after the internal loops 758 of the GMCA corrected most of the overestimation of the 759 spectrum caused by the leakage, and improved the retrieved 760 temperatures.

– **Block Bootstrap:** Spectral analyzing tools such as **Xspec** 763 need error bars in order to fit physical models. The Block 764 Bootstrap resampling method tested here is a promising way 765 to estimate error bars from a single set of data.

– **Performance:** The ability of the GMCA to disentangle 766 components depends on the total number of counts in the data, on 767 the number of counts of each component and on the nature 768 of the data itself: performance is very case-specific. In this 769 paper, we focused on the study of highly spatially entangled 770 sources, which is frequent in the study of SNRs, and which is 771 an extremely challenging analysis task. For that reason, the 772 weakest ratio at which every component could be success- 773 fully retrieved depends on the morphological and spectral 774 diversity. We also note that the algorithm is more successful 775 in finding faint features when applied in narrow, targeted en- 776 ergy bands rather than when applied to the full energy range. 777 To conclude, GMCA is a fast running algorithm, taking only 778 a few minutes to extract sources from a $200 \times 200 \times 300$ data 779 cube on a single core personal computer.

The version of GMCA we used in this study had originally 782 been developed to handle the Gaussian noise in *Planck* data. 783 The method will be enhanced in future work by inclusion of a 784 treatment for Poisson statistics that should help retrieving fainter 785 components and diminishing leakages. In addition, exposure and 786 background cubes will be implemented for application of the 787 method to large mosaic observations. The use of physically- 788 motivated spectral models to guide the component separation 789 process could also be envisaged.

New spectro-imaging instruments with increased effective 791 area and high spectral resolution, such as *Athena*, will provide 792

793 data whose tremendous potential cannot be fully exploited with
 794 existing data analysis methods. The GMCA provides a new way
 795 to leverage all possible dimensions in the data, thus allowing a
 796 maximum of physical information to be obtained.

797 *Acknowledgements.* This research made use of Astropy,⁴ a community-
 798 developed core Python package for Astronomy (Astropy Collaboration et al.
 799 2013, 2018). GWP acknowledges funding from the European Research Coun-
 800 cil under the European Union’s Seventh Framework Programme (FP7/2007-
 801 2013)/ERC grant agreement No. 340519. JB acknowledges funding from the Eu-
 802 ropean Community through the grant LENA (ERC StG - contract no. 678282).

803 References

- 804 Astropy Collaboration, Price-Whelan, A. M., Sipőcz, B. M., et al. 2018, AJ, 156,
 805 123
 806 Astropy Collaboration, Robitaille, T. P., Tollerud, E. J., et al. 2013, aap, 558, A33
 807 Bobin, J., Rapin, J., Larue, A., & Starck, J.-L. 2015, IEEE Transactions on Signal
 808 Processing, 63, 1199
 809 Bobin, J., Sureau, F., & Starck, J.-L. 2016, A&A, 591, A50
 810 DeLaney, T., Rudnick, L., Stage, M. D., et al. 2010, ApJ, 725, 2038
 811 Diehl, S. & Statler, T. S. 2006, MNRAS, 368, 497
 812 Efron, B. 1979, Volume 7, Number 1, 1-26
 813 Fadili, J., Starck, J.-L., & Murtagh, F. 2007, The Computer Journal, Oxford Uni-
 814 versity Press (UK), pp.64
 815 Jones, D. E., Kashyap, V. L., & van Dyk, D. A. 2015, ApJ, 808, 137
 816 Starck, J.-L., Fadili, J., & Murtagh, F. 2007, IEEE Transactions on Image Pro-
 817 cessing, 16, 297
 818 Starck, J.-L., Murtagh, F., & Fadili, J. 2015, Sparse Image and Signal Processing:
 819 Wavelets and Related Geometric Multiscale Analysis, 2nd edn. (Cambridge
 820 University Press)
 821 Wang, Z., Bovik, A., Sheikh, H., & Simoncelli, E. 2004, IEEE Transactions on
 822 Image Processing
 823 Warren, J. S., Hughes, J. P., & Badenes, C. 2005, in Bulletin of the American
 824 Astronomical Society, Vol. 37, American Astronomical Society Meeting Ab-
 825 stracts, 1437
 826 Willingale, R., Bleeker, J. A. M., van der Heyden, K. J., Kaastra, J. S., & Vink,
 827 J. 2002, A&A, 381, 1039

⁴ <http://www.astropy.org>

828 Appendix A: Wavelets and Starlets

829 A wavelet is a square-integrable function of zero mean. Ba-
 830 sically, a wavelet transform consists in contracting a mother
 831 wavelet and convolving it with an image, each scale providing
 832 a new image. Each wavelet scale contains informations about
 833 structures of a specific size. For that reason, a wavelet trans-
 834 form proves useful to disentangle components using their mor-
 835 phological specificities. The starlet transform is a special case of
 836 bi-dimensional wavelets, which have been specifically designed
 837 to efficiently represent isotropic structures in images. Therefore,
 838 this particular case of wavelets has been proved to be well-
 839 adapted to analyze astrophysical images.

The Starlet transform first builds a sequence of approxima-
 tions of an $n \times n$ image c_0 at increasingly larger scales $\{c_1, \dots, c_J\}$.
 Each approximation is obtained from the previous one through a
 convolution with a mother wavelet filter $\bar{h}^{(j)}$ at scale $j + 1$:

$$c_{j+1}[k, l] = (\bar{h}^{(j)} \star c_j)[k, l], \quad (\text{A.1})$$

840 where the filter $h^{(0)}$ is defined as :

$$h^{(0)} = \frac{1}{256} \begin{pmatrix} 1 & 4 & 6 & 4 & 1 \\ 4 & 16 & 24 & 16 & 4 \\ 6 & 24 & 36 & 24 & 6 \\ 4 & 16 & 24 & 16 & 4 \\ 1 & 4 & 6 & 4 & 1 \end{pmatrix} \quad (\text{A.2})$$

841 According to the "à trous" algorithm, consecutive filters are $h^{(j)}$
 842 are obtained by adding zeroes between the nonzero filter ele-
 843 ments so as to dilate the filter by a factor 2 from scale to scale
 844 Starck et al. (2015).

The wavelet coefficient at scale $j + 1$ is then defined as the
 difference between consecutive large-scale approximations:

$$w_{j+1}[k, l] = c_j[k, l] - c_{j+1}[k, l] \quad (\text{A.3})$$

845 This eventually yields a decompostion of the image c_0 into a
 846 coefficient set $W = \{w_1, \dots, w_J, c_J\}$.

847 The reconstruction of the initial image c_0 is then obtained by
 848 a simple coaddition of all wavelet scales and the final smooth
 849 subband :

$$c_0[k, l] = c_J[k, l] + \sum_{j=1}^J w_j[k, l] \quad (\text{A.4})$$

850 In Figure A.1, we build a very simple toy model to show the
 851 relevance of starlet transforms to separate components in a cube
 852 (E, x, y). The data cube is the sum of two components: an array
 853 of small spatial gaussians multiplied by a flat spectrum and a
 854 large spatial gaussian multiplied by a spectral line. A gaussian
 855 noise with a standard deviation of 2/pixel is added to the cube.
 856 The figure points out the differences between the coefficients of
 857 the two components in the third starlet scale.

858 Appendix B: Spatial and spectral accuracy

859 In this section we see some additional figures resulting from our
 860 tests of the GMCA on our first two toy models. Figure B.1 shows
 861 examples of images of the Fe spatial distribution in our first toy
 862 model by GMCA and an interpolation method for three different
 863 ratios Fe line/Synchrotron, and the corresponding SSIM coef-
 864 ficients. Figure B.2 shows the evolution of the accuracy of the
 865 retrieved images for 15 ratios in our first and second toy models

with a total count corresponding to a 100 ks observation. Fig-
 866 ure B.3 shows the parameters of the Fe K gaussian in our first
 867 toy model as retrieved by Xspec without using GMCA. It offers
 868 a good comparison with Figure 3, where the parameters were
 869 retrieved by fitting the spectra given by GMCA. 870

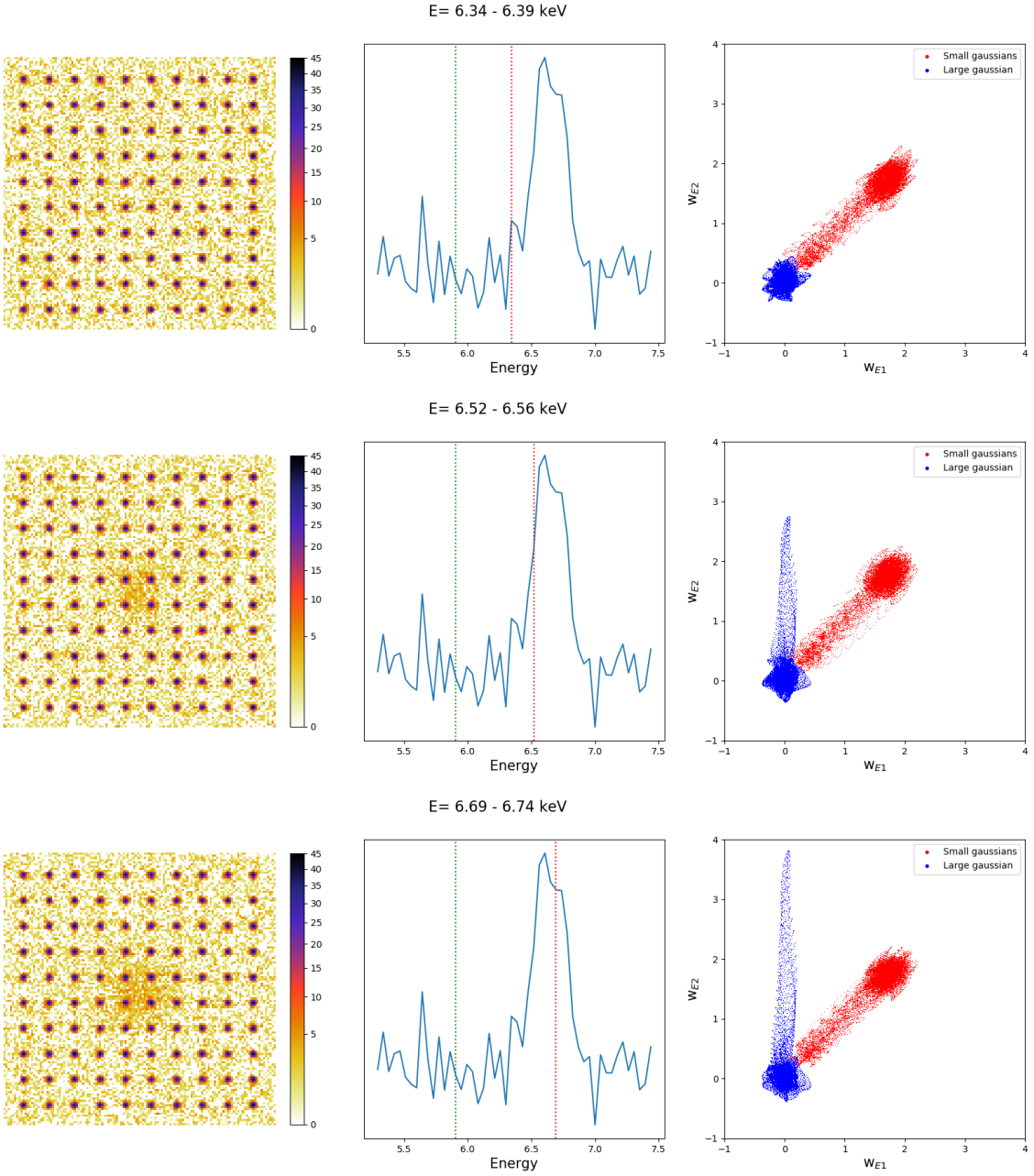


Fig. A.1: An illustration of the relevance of wavelet transforms to separate components in a cube (E, x, y) using a simple toy model. On the left, the slice of the cube at the current energy E_2 . In the center, the total spectrum. The green line corresponds to E_1 while the red one corresponds to E_2 . On the right, a representation of the coefficients of both components in the third wavelet scale at E_2 as a function of the coefficients of both components in the third wavelet scale at E_1 . It appears clearly that the coefficients of the two components are clearly dissociated in the wavelet space, whereas their images are tightly entangled.

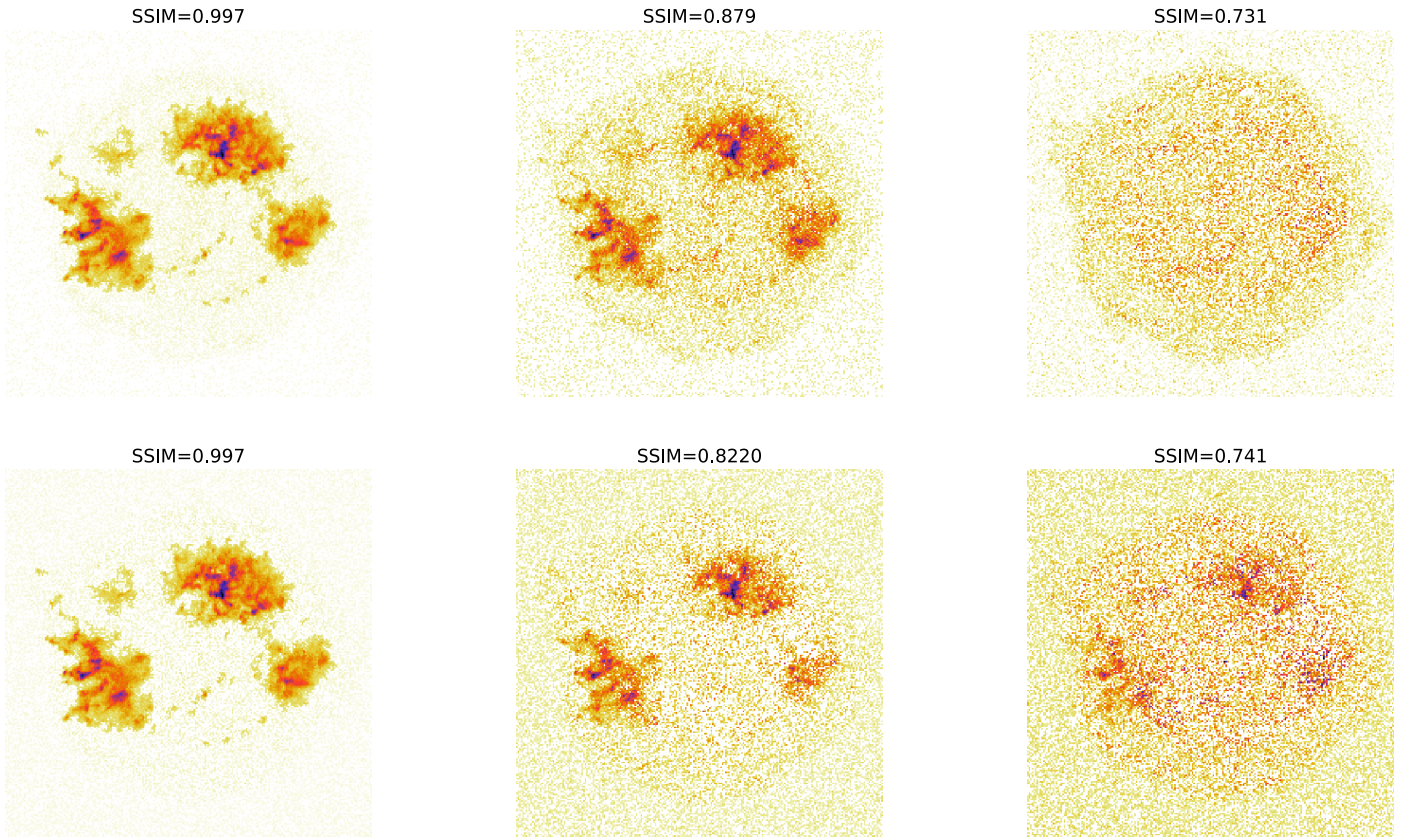


Fig. B.1: Images of the Fe spatial structures in our first toy model as found by GMCA without fixing the Fe spectral shape (on top) and by an interpolation method (below) for the three ratios Fe Line/Synchrotron marked by arrows in Figure 2). The SSIM coefficients are written on top of the images. Coefficients under 0.75 describe images where the Fe structures are not recognizable, but the SSIM is still high because of the similarities between intrinsic Fe and synchrotron distributions.

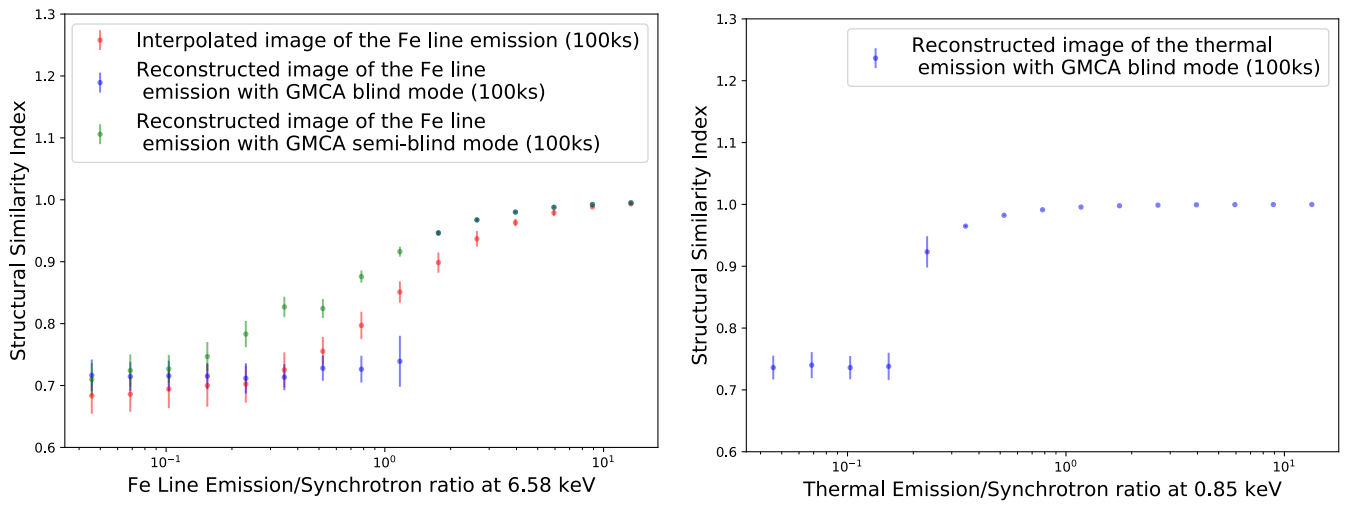


Fig. B.2: SSIM coefficients of the input and output images found by GMCA for a total number of counts corresponding to a 100 ks observation. The points are the average of all Monte-Carlo realizations at a particular ratio, and the error bars the standard deviation of those realizations. On the left, a comparison of the image quality obtained in retrieving the Fe structure in our first toy model for different ratios Line emission/Synchrotron, between an interpolation method, a GMCA in blind mode and a GMCA in semi-blind mode. On the right, the image quality of the thermal emission structure retrieved for different ratios by a GMCA in blind mode.

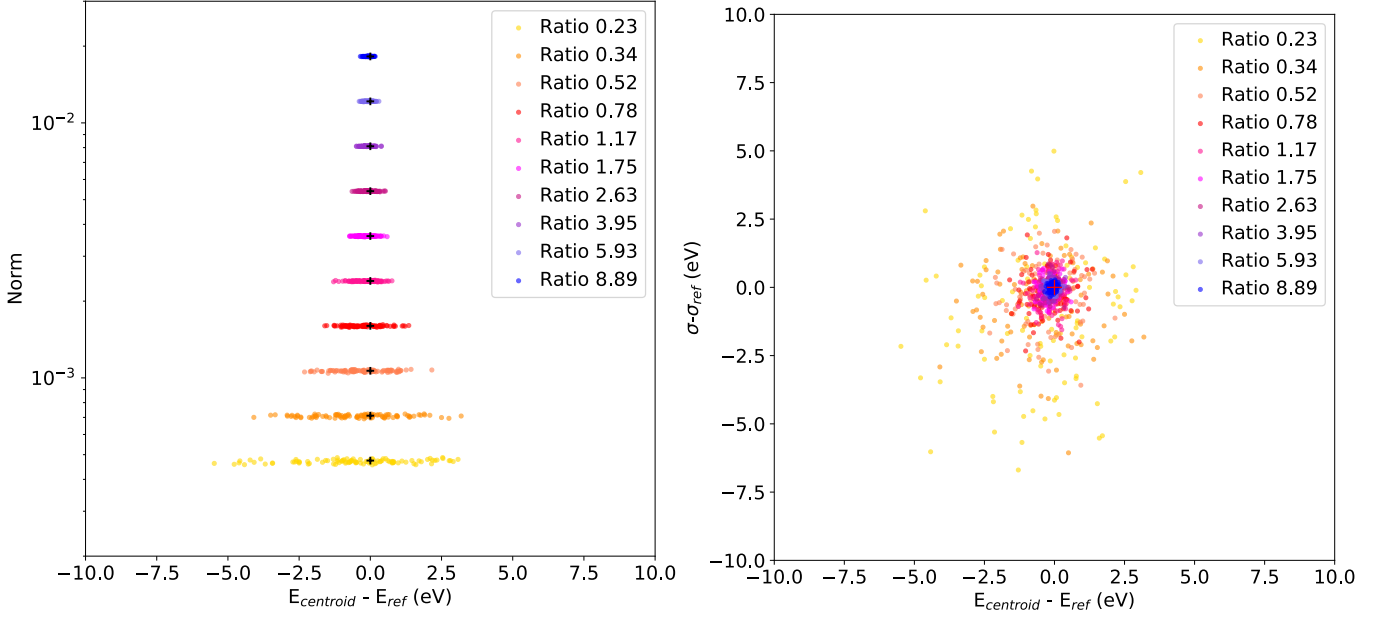


Fig. B.3: Parameters of the Fe K gaussian as retrieved by Xspec on our first toy model's total spectrum for a hundred realizations of each out of ten different Fe Line/Synchrotron ratios with a total number of counts corresponding to a 1 Ms observation. On the left, the retrieved E_c and σ . On the right, the retrieved norm and E_c . In both cases, the theoretical results are represented by black crosses.